ChemPubSoc Europe

DOI: 10.1002/open.201800091

Open Access ChemistryOPEN Full Papers

Mechanochemical Synthesis of Iron and Cobalt Magnetic Metal Nanoparticles and Iron/Calcium Oxide and Cobalt/Calcium Oxide Nanocomposites

Varun Chaudhary,*[a] Yaoying Zhong,[a] Harshida Parmar,[a] Vinay Sharma,[a] Xiao Tan,[a] and Raju V. Ramanujan*[a, b]

We report an environmentally benign and cost-effective method to produce Fe and Co magnetic metal nanoparticles as well as the Fe/Cao and Co/CaO nanocomposites by using a novel, dry mechanochemical process. Mechanochemical milling of metal oxides with a suitable reducing agent resulted in the production of magnetic metal nanoparticles. The process involved grinding and consequent reduction of low-costing oxide powders, unlike conventional processing techniques involving metal salts or metal complexes. Calcium granules were used as the reducing agent. Magnetometry measurements were performed over a large range of temperatures, from 10 to 1273 K, to evaluate the Curie temperature, blocking temperature, irreversibility temperature, saturation magnetization, and coercivity. The saturation magnetizations of the iron and cobalt nanoparticles were found to be 191 and 102 emu g^{-1}, respectively. The heating abilities of these nanoparticles suspended in several liquids under alternating magnetic fields were measured and the specific loss power was determined. Our results suggest that the dry mechanochemical process is a robust method to produce metallic nanoparticles and nanocomposites.

1. Introduction

Magnetic nanoparticles are used in a variety of applications, for example, catalysis, biomedicine, optoelectronics, magnetic recording media, magnetic fluids, and rechargeable batteries.[1–3] Such nanoparticles are useful in areas such as the separation of catalysts, nuclear waste, biochemical products, and biological entities such as cells.[1,4] For example, an advantage of magnetic nanoparticles is the facile recovery of nanocatalysts in a liquid-phase reaction by an external magnet compared to conventional methods of filtration and centrifugation.

Iron and cobalt metallic magnetic nanoparticles have been less studied than their oxides and alloys.[5–11] The major reason for this is that these nanoparticles are pyrophoric and, hence, are difficult to synthesize. Cobalt nanoparticles have been proposed as a cheaper alternative to the much more expensive metal platinum for catalysis.[12,13]

Fe/CaO nanocomposite materials have been used for the separation and immobilization treatment of dry soil contaminated by radioactive cesium.[14] Calcium oxide is catalytically active, and the magnetic iron component is used to separate the catalyst magnetically so that it can be recycled. Iron nanoparticles have higher magnetic moments than iron oxides, and this makes them more useful in applications such as magnetic separation and targeted drug delivery, for which a magnetic force is applied by an external magnetic field gradient to manipulate the particles.[7] For such applications, superparamagnetic nanoparticles are often embedded in a matrix to form a core–shell structure that can be functionalized by a biologically active entity.

Both Fe and Co nanoparticles can be physically blended with Nd-Fe-B hard magnetic nanoparticles to form exchange coupled hard–soft magnets exhibiting a giant energy product.[15] The addition of Fe (or Co) can significantly improve the magnetic properties due to enhanced interdiffusion across the Nd-Fe-B/Fe (or Nd-Fe-B/Co) interfaces, which increases interphase exchange coupling.

If magnetic nanoparticles are dispersed in a solution and subjected to an alternating magnetic field (AMF), they can convert electromagnetic energy into heat. This property of magnetic nanoparticles can be used for several applications, including biomedicine,[16,17] smart windows, and other applications for which local heating is advantageous.[18] Hence, magnetic

[a] Dr. V. Chaudhary, Y. Zhong, Dr. H. Parmar, V. Sharma, X. Tan, Prof. R. V. Ramanujan
School of Materials Science and Engineering
Nanyang Technological University
Singapore 639798 (Singapore)
E-mail: varun004@e.ntu.edu.sg

[b] Prof. R. V. Ramanujan
Singapore-HUJ Alliance for Research and Enterprise (SHARE)
Nanomaterials for Energy and Energy-Water Nexus (NEW)
Campus for Research Excellence and Technological Enterprise (CREATE)
Singapore 138602 (Singapore)
E-mail: ramanujan@ntu.edu.sg

Supporting Information and the ORCID identification number(s) for the author(s) of this article can be found under: https://doi.org/10.1002/open.201800091.

nanoparticles that exhibit high heating efficiency at a reasonable frequency and a low alternating magnetic field strength are of high interest.

The synthesis of stable magnetic nanoparticles by a cost-effective route is a current challenge. Various techniques have been attempted to prepare metal nanoparticles, including high-temperature thermal decomposition, vapor-phase condensation, and hydrogen reduction.[1,7] Metal carbonyl pyrolysis has been used to produce Fe and Co nanoparticles.[19,20] However, high-temperature reactions, multistep processes, toxic chemicals, hazardous starting materials (such as hydrogen), and the extensive labor needed resulting in high costs are all limitations of these techniques.

The reduction of iron/cobalt oxides to iron/cobalt nanoparticles is not commonly performed, as it is difficult to solubilize these oxides in solvents; therefore, they cannot be easily reduced to their zero-valent state.[7] The industrial process to form Fe particles involves the precipitation of iron hydroxide and dehydration of the hydroxide to form iron oxide, followed by reduction by hydrogen gas to form the desired iron particles. In our present method, which is a dry and "green" mechanochemical processing technique, there is no need to solubilize the oxides in a solvent.[21] This technique can be used to reduce iron and cobalt to their zero-valent state by calcium rather than by hydrogen.

Mechanochemistry has been used since the very early history of humankind.[22] The introduction of fire by hitting two flints is one of the oldest, most beautiful, and basic examples of mechanochemistry. Ball milling with the use of mechanical energy to initiate reactions has been used to develop a wide range of materials, including oxides, compounds, alloys, functional materials, and core–shell materials.[23,24] Metallic nanoparticles, oxide nanoparticles, and nanocomposites produced by mechanochemical processing are summarized in Table 1.

Recently, the mechanochemical approach has been used to synthesize catalysts,[35,36] magnets,[21,37,38] γ-graphyne,[39] metal iodates,[40] $CuFeS_2$ particles,[41] nickel–vanadium carbide,[42] and molybdenum–vanadium carbide nanocomposite powders.[43]

We report the synthesis of Fe and Co nanoparticles as well as their nanocomposites with CaO by mechanochemical processing. We used commonly occurring, inexpensive metal oxides as starting materials rather than the usual metal salts or metal acetylacetonate/carbonyl complexes.[26,44–46] This mechanochemical technique to prepare metal nanoparticles by using easily available oxides and no toxic solvents is novel and scalable. Another advantage is that it can be used to recycle the oxidized nanoparticles back to metal nanoparticles without the need for chemical solvents or multistep processes.

2. Results and Discussion

2.1. Structural Analysis

The XRD pattern of the Fe/CaO nanocomposite shows diffraction peaks associated with the α-Fe and CaO phases, which indicates that Fe_2O_3 is reduced to Fe and that Ca is oxidized to CaO (Figure 1 a). The mass fraction of these phases, calculated by Rietveld refinement, shows that the Fe/CaO nanocomposite exhibits a major phase of CaO (85.5 %) and a minor phase of α-Fe (14.5 %). Zamboni et al. reported that such Fe/CaO composite powders can be used for CO_2 absorption and tar removal in biomass gasification.[47] The α-Fe phase possesses lattice parameters of $a = 2.86905(5)$ Å, $V = 23.6165(7)$ Å^3, and $Z = 2$ and the $Im\bar{3}m$ space group. The CaO phase has lattice parameters of $a = 4.81703(5)$ Å, $V = 111.7736(6)$ Å^3, and $Z = 4$ and the $Fm\bar{3}m$ space group. The XRD patterns of the nanoparticles obtained after removal of CaO from the Fe/CaO nanocomposite by methanol and ammonium chloride reveal α-Fe diffraction

Table 1. Summary of mechanochemical reactions of metal nanoparticles, oxide nanoparticles and nanocomposites.

Nanoparticles/nanocomposite	Mechanochemical reaction	Ref.
Metal nanoparticles		
iron	$FeCl_3 + 3\,Na \rightarrow Fe + 3\,NaCl$	[25]
cobalt	$CoCl_2 + 2\,Na \rightarrow Co + 2\,NaCl$	[25]
copper	$CuCl_2 + 2\,Na \rightarrow Cu + 2\,NaCl$	[25]
nickel	$CuCl_2 + 2\,Na \rightarrow Cu + 2\,NaCl$	[25,26]
Oxide nanoparticles		
aluminum oxide	$2\,AlCl_3 + CaO \rightarrow Al_2O_3 + 3\,CaCl_2$	[27]
zirconium oxide	$ZrCl_4 + 2\,CaO \rightarrow ZrO_2 + 2\,CaCl_2$	[28]
zinc oxide	$ZnCl_2 + Na_2CO_3 + 6\,NaCl \rightarrow ZnO + 8\,NaCl + CO_2$	[29]
gadolinium oxide	$GdCl_3 + 3\,NaOH \rightarrow Gd_2O_3 + 3\,NaCl + 1.5\,H_2O$	[25]
iron oxide	$2\,FeCl_3 + 3\,Ca(OH)_2 \rightarrow Fe_2O_3 + 3\,CaCl_2 + 3\,H_2O$	[25]
iron oxide	$3\,Na_2CO_3 + 2\,FeCl_3{\cdot}6\,H_2O \rightarrow 6\,NaCl + Fe_2O_3{\cdot}6\,H_2O + 3\,CO_2$	[30]
Metal–metal oxide nanocomposite		
iron–copper oxide	$4\,CuO + 3\,Fe \rightarrow Fe_3O_4 + 4\,Cu$	[31]
iron–alumina	$3\,Fe_3O_4 + 8\,Al \rightarrow 9\,Fe + 4\,Al_2O_3$	[32,33]
iron–zinc oxide	$Fe_3O_4 + 4\,Zn \rightarrow 3\,Fe + 4\,ZnO$	[32,34]

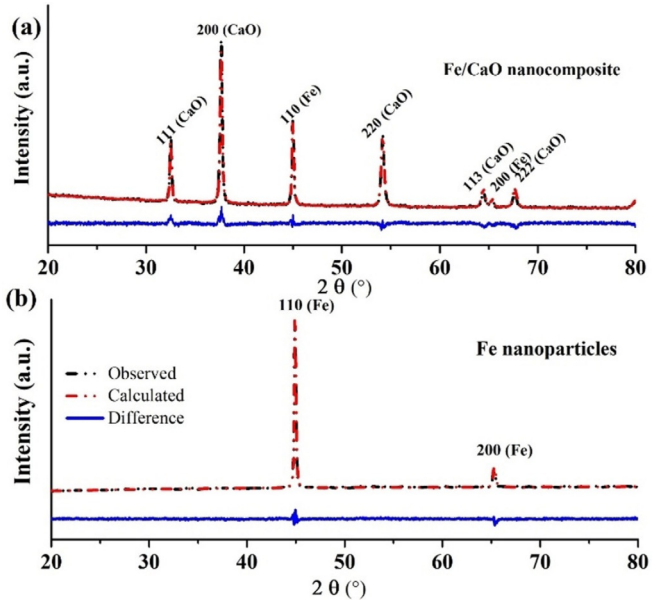

Figure 1. Rietveld refinement of the powder X-ray diffraction patterns of a) the Fe/CaO nanocomposite and b) Fe nanoparticles. The observed counts and calculated patterns are indicated by black and red dashed lines, respectively. The bottom blue trace indicates the difference between the observed and calculated values.

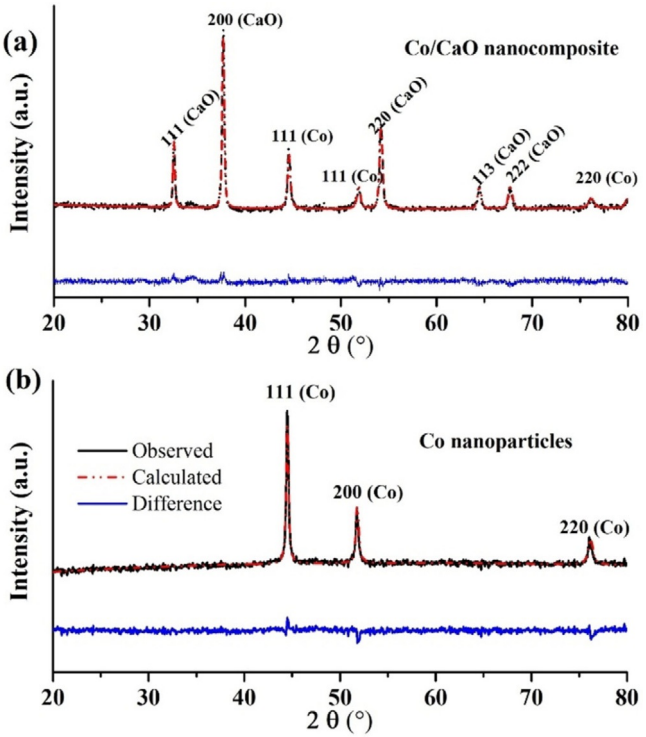

Figure 2. Rietveld refinement of the powder X-ray diffraction patterns of a) the Co/CaO nanocomposite and b) Co nanoparticles. The observed counts and calculated patterns are indicated by black and red dashed line, respectively. The bottom blue trace indicates the difference between the observed and calculated values.

peaks (Figure 1 b). α-Fe has lattice parameters of $a=$ 2.86427(2) Å, $V=23.4986(5)$ Å^3, and $Z=2$ and the $Im\bar{3}m$ space group. The small change in the unit-cell parameters after removal of CaO may be associated with a change in surface energy.[48] The average crystallite size (D) was estimated from the Scherrer formula [Eq. (1)]:

$$D = \frac{0.9\lambda}{(B\cos\theta)} \quad (1)$$

in which λ is the wavelength of the X-rays and B is the corrected full width at half maximum (FWHM) of the diffraction peak taking silicon as the standard.[49,50] The average crystalline size of the Fe powders is 33 nm.

Figure 2 a shows that the XRD pattern of the Co/CaO nanocomposite matches the standard diffraction patterns of Co and CaO, which indicates that CoO is completely reduced to Co and that Ca is oxidized to CaO. Rietveld refinement shows that the Co/CaO nanocomposite exhibits a major phase of CaO (79.2 %) and a minor phase of Co (20.8 %). Co has lattice parameters of $a=3.54855(5)$ Å, $V=44.6842(9)$ Å^3, and $Z=4$ and the $Fm\bar{3}m$ space group. CaO has lattice parameters of $a=$ 4.81634(2) Å, $V=111.7254(7)$ Å^3, and $Z=4$ and the $Fm\bar{3}m$ space group. The XRD patterns of the powder, after removal of CaO from Co/CaO, show diffraction peaks associated with Co (Figure 2 b). Co has lattice parameters of $a=3.54050(7)$ Å, $V=$ 44.3809(6) Å^3, and $Z=4$ and the $Fm\bar{3}m$ space group. The unit-cell volume for cobalt is slightly less than that for cobalt in the Co/CaO composite, as in the case of iron. The average crystalline size of the Co nanoparticles, calculated by the Scherrer formula, is 22 nm.

Figure 3 shows the TEM images, selected area electron diffraction (SAED) patterns, and histograms of the particle-size distribution for Fe and Co nanoparticles. Nanoparticles with an equiaxed shape are observed in both the Fe and Co nanoparticles. The size distribution of the iron nanoparticles is in the range of 7 to 90 nm, with an average size of 29 nm (inset of Figure 4 a), whereas the size distribution of the cobalt nanoparticles is in the range of 5 to 50 nm, with an average size of 18 nm. The SAED patterns of the Fe (Figure 3 a_2) and Co (Figure 3 b_2) samples are consistent with the XRD results. Any processing parameters, such as the size of the milling media or milling time, that influence the grain size within the particles may also have an effect on the particle size.[51,52] The SAED patterns in both (Fe and Co nanoparticles) cases exhibit rings with bright spots, which confirm the polycrystalline nature of nanoparticles. We indexed the SAED pattern and found that Fe and Co exhibit body centered cubic (BCC) and face centered cubic (FCC) crystal structures; these structures are consistent with the obtained structures from XRD.

After milling, the black powder was collected in an argon glovebox and was pressed into a pellet by using a hydraulic press to minimize exposure of the powder to air. This pellet was heat treated in a tube furnace at 850 °C for 90 min under high vacuum ($\approx 10^{-5}$ Torr; 10 Torr = 1.3 kPa). The heat-treated samples could then be handled in air. Heat treatment may be the reason that our particles are larger than what was achieved earlier, as those particles were not annealed.

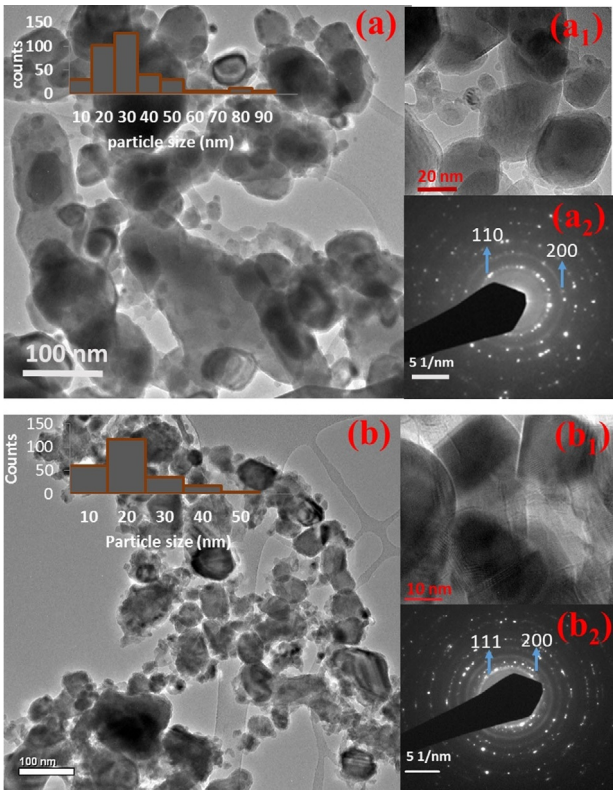

Figure 3. Bright-field transmission electron micrographs of a) Fe nanoparticles and b) Co nanoparticles; the insets show the histograms of the average particle-size distributions. a_1, b_1) High-resolution transmission electron micrographs and a_1, b_2) SAED of the corresponding Fe and Co nanoparticles, respectively.

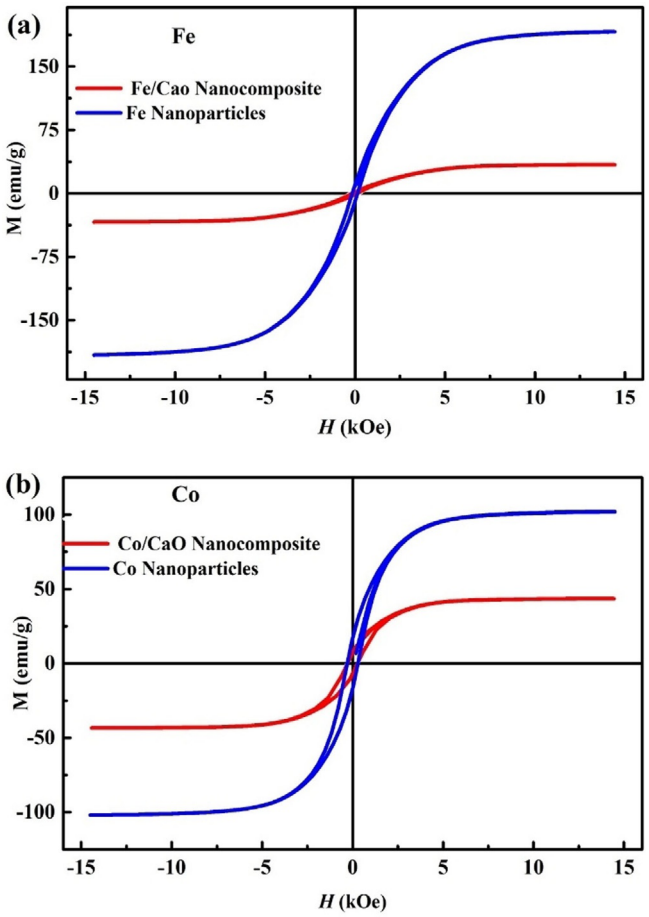

Figure 4. Magnetization versus magnetic field hysteresis loop measured at room temperature for a) the Fe/CaO nanocomposite (red) and Fe nanoparticles (blue) and b) the Co/Cao nanocomposite (red) and Co nanoparticles (blue).

The synthesis of tin-oxide nanoparticles by mechanochemical reaction of $SnCl_2$ and Na_2CO_3 with NaCl as a diluent and subsequent thermal treatment resulted in SnO_2 nanocrystallites with an average crystal size in the size range of 25 to 40 nm.[53] The particle sizes of mechanochemical products can vary over a large range.[21,25,26,37,52,54]

2.2. Room-Temperature Magnetic Properties

Figure 4a shows the room-temperature magnetic hysteresis loops of the Fe/CaO nanocomposite and the Fe powders.

The saturation magnetization (M_S) of the Fe/CaO nanocomposite was found to be 34 emu g^{-1}. Rietveld refinement revealed that this sample contained CaO as the major phase. The M_S value of our Fe nanoparticles measured at room temperature was found to be 219 emu g^{-1}, which confirmed the metallic character of the Fe nanoparticles, as the M_S of iron oxides can reach a maximum value of 84 emu g^{-1}. Enhanced spin disorder at the particle surfaces is common in magnetic nanoparticles, and therefore, the surface atoms experience anisotropy due to the broken symmetry of their surroundings, called Neel surface anisotropy.[55,56] Therefore, the fact that the M_S value of our nanoparticles is lower than that of the bulk counterpart can be attributed to the broken symmetry at the particle surfaces.

The coercivity values of the Fe/CaO nanocomposite and Fe powders were found to be 144 and 152 Oe, respectively. Figure 4b shows the magnetic hysteresis loops of the Co/CaO nanocomposite and Co powders at room temperature. All samples displayed typical ferromagnetic characteristics. The M_S values of the Co/CaO nanocomposite and Co powders were found to be 42 and 102 emu g^{-1}, respectively. The M_S value of the cobalt nanoparticles was lower than that of bulk cobalt (162 emu g^{-1}). The coercivity values of the Co/CaO nanocomposite and Co nanoparticles were found to be 269 and 294 Oe, respectively.

The M_S and coercivity (H_C) of the cobalt nanoparticles varies with the particle size in a nonlinear fashion and depends on the synthesis route, heat treatment parameters, precursors, solvents used, and so on. Domain walls appear if the size of the particles increases above a critical size, and the particles become multidomain with mobile domain walls. The critical size depends on the anisotropy energy, exchange interaction, and saturation magnetization. Kahani et al. prepared cobalt nanoparticles through the intermolecular reaction of cobalt complexes[57] and found that the M_S was in the range of 68 to 135 emu g^{-1}, depending on the conversion of the cobalt com-

plexes and other reaction parameters. The EDX results (Figure S1 and Table S1) show the presence of Ca(O) in the Co nanoparticle sample, which may be another reason for the reduced value of the saturation magnetization.

2.3. High-Temperature Magnetic Properties

Figure 5 shows the temperature dependence of magnetization [$M(T)$] of the Fe nanoparticles under a field of 0.1 T. The Curie temperature (T_C) of the Fe nanoparticles was found to be 923 K, as determined by the point of intersection of the two

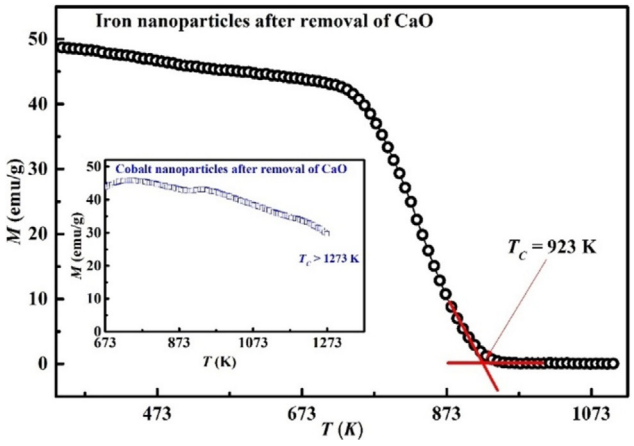

Figure 5. Magnetization as a function of temperature [$M(T)$] for iron nanoparticles at $\mu_0 H = 0.1$ T. Inset shows the $M(T)$ of cobalt nanoparticles at $\mu_0 H = 0.1$ T.

tangents around the inflection point of the $M(T)$ curve. The T_C of our Fe nanoparticles is 120 K less than that of the bulk Fe counterpart. This reduction in the T_C may be associated with the reduced coordination number of the surface atoms of the nanoparticles, which can lead to a difference in cohesive energy between the surface atoms and bulk atoms.[58] It was previously observed experimentally and theoretically that the T_C values of Fe, Ni, and Co nanoparticles were less than those of the bulk counterparts.[58–60] We measured the temperature dependence of magnetization [$M(T)$] of the Co nanoparticles (inset of Figure 5). The T_C of the Co nanoparticles was greater than 1273 K, as there was no transition up to this temperature. This finding suggests that the sample is pure cobalt nanoparticles, as cobalt-based alloys or oxides have T_C values less than 1273 K.

2.4. Low-Temperature Magnetic Properties

Figure 6 shows the zero-field-cooling (ZFC) and field-cooling (FC) magnetization curves for the iron and cobalt nanoparticles as a function of temperature. In the ZFC measurements, the nanoparticles were cooled from 400 to 10 K in the absence of an applied magnetic field. After reaching 10 K, the magnetization was determined as a function of increasing temperature under an external magnetic field. For the FC measurements, the nanoparticles were cooled from 400 to 10 K under an ap-

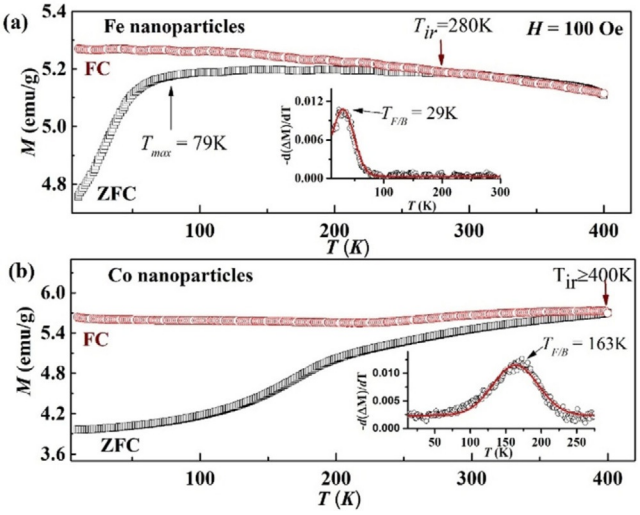

Figure 6. Zero-field-cooling and field-cooling (ZFC-FC) magnetization curves for a) Fe nanoparticles and b) Co nanoparticles at an applied magnetic field of 100 Oe. The insets show the derivatives of the differences of the magnetization of the ZFC and FC curves versus temperature.

plied magnetic field of 100 Oe. Subsequently, the magnetization was recorded with increasing temperature, from 10 to 400 K. After cooling to 10 K, without an applied field, the magnetic moments were randomly oriented. At low temperatures, an applied magnetic field forces the reorientation of the moments of the individual particles along the applied magnetic field.[61] Therefore, the ZFC magnetization increases with increasing temperature and reaches a maximum at a temperature denoted as T_{max}.

The T_{max} of the iron nanoparticles at an applied magnetic field of 100 Oe was found to be 79 ± 4 K. The ZFC and FC magnetizations merge at the temperature of irreversibility (T_{ir}), which is related to the blocking temperature for the larger particles in the sample.[62] The T_{ir} values for the iron and cobalt nanoparticles at an applied magnetic field of 100 Oe were found to about 280 and ≥400 K, respectively. For both materials, the T_{ir} value was larger than the temperature at which the magnetization became a maximum (T_{max}). This behavior of the ZFC–FC curves indicates strong dipole–dipole interactions among the particles due to particle aggregation and to the polydispersity of the particles.[63]

To determine the mean spin freezing/blocking temperature ($T_{F/B}$), the derivative of the difference in the magnetization values of the ZFC and FC curves with respect to temperature, that is, $-\mathrm{d}(\Delta M)/\mathrm{d}T$ (inset of Figure 6a,b) was measured, for which $\Delta M = M_{FC} - M_{ZFC}$. The curve displays a log-normal blocking temperature distribution function. The values of the mean blocking temperature ($T_{F/B}$) and the standard deviations in $\ln(T_{F/B})$ were found to be 29 and 163 K and 0.5 and 0.4 for the Fe and Co nanoparticles, respectively. The anisotropy of the Fe and Co nanoparticles was calculated by using Equation (2):[64]

$$H_c = \frac{2K}{M_S} \quad (2)$$

in which K is the magnetic anisotropy and was found to be 2.9×10^3 J m^{-3} for the Fe nanoparticles and 3.0×10^3 J m^{-3} for the Co nanoparticles. The calculated anisotropy values for our nanoparticles are lower than those of the corresponding bulk values, as the magnetic anisotropy (K) depends on the particle size, shape, microstructure, interparticle interactions, and intraparticle interactions or dipole–dipole interactions. Yang et al. reported $T_B = 92$ K for 7 nm cobalt nanoparticles deposited on a pyrolytic graphite substrate.[65] The higher value of T_B for our cobalt nanoparticles is due the larger particle size, as T_B is a function of the particle volume.

2.5. Heating Efficiency under Alternating Magnetic Field

In an alternating magnetic field (AMF), bare magnetic particles or magnetic particles suspended in a suitable liquid carrier medium absorb energy from the AMF and convert this energy into heat by relaxation losses or eddy current losses. These losses can be quantified by the specific loss in power (SLP) by using the following relationship [Eq. (3)]:

$$\mathrm{SLP} = \frac{c_{\mathrm{solvent}} m_{\mathrm{solvent}}}{m_{\mathrm{nanoparticles}}} \left(\frac{\mathrm{d}T}{\mathrm{d}t}\right) \quad (3)$$

in which c_{solvent} is the specific heat capacity of the solvent, m_{solvent} is the total mass of the sample, $m_{\mathrm{nanoparticles}}$ is the mass of nanoparticles in the solvent, and $\mathrm{d}T/\mathrm{d}t$ is the slope of the heating curve.[66,67]

First, the Fe and Co nanoparticles were subjected to an AMF. It was found that the SLP was higher for the Fe nanoparticles than for the Co nanoparticles. The SLP of the Fe nanoparticles was found to be 25 W g^{-1}, whereas the SLP for the Co nanoparticles was 7 W g^{-1}. Hence, Fe nanoparticles were chosen for additional AMF studies.

The SLP of Fe nanoparticles dispersed in different solvents was investigated (Figure 8a). All of the samples were prepared by using 0.2% (*v*/*v*) Fe nanoparticles in the solvent. It was observed that Fe nanoparticles in ethylene glycol (EG) and light mineral oil (LMO) showed less heating than nanoparticles in oleic acid (OA). After 240 s, the maximum temperatures of the iron nanoparticles in EG, LMO, and OA were 69, 75, and 98 °C, respectively. The inset of Figure 7a shows the SLP for the Fe nanoparticles in these three solvents. As the SLP depends on the initial slope of the temperature versus time curve, the performance of oleic acid was the highest among these solvents. A SLP value of 47 W g^{-1} was observed for the Fe nanoparticles dispersed in OA. The SLP of $CoFe_2O_4$ nanoparticles at a frequency of 763 kHz and a field strength of 3 kA m^{-1} was 0.25 W g^{-1}.[68] Bekovic and Hamler reported a SLP value of 0.5 W g^{-1} at a frequency of 185 kHz and a field strength of 2.3 kA m^{-1} for γ-Fe_2O_3 dispersed in mineral oil.[66] Other groups reported higher SLP values reaching 1000 W g^{-1} for iron-oxide nanoparticles, but the field strength was high ($\approx$24 kA m^{-1}).[69] Therefore, exact comparison of the experimental SLP values with those found in the literature is difficult, as it depends on several factors, including particle concentration, solvent type, applied frequency, and field strength, but in general, our iron nanoparticles showed promising SLP at low frequency and low field.

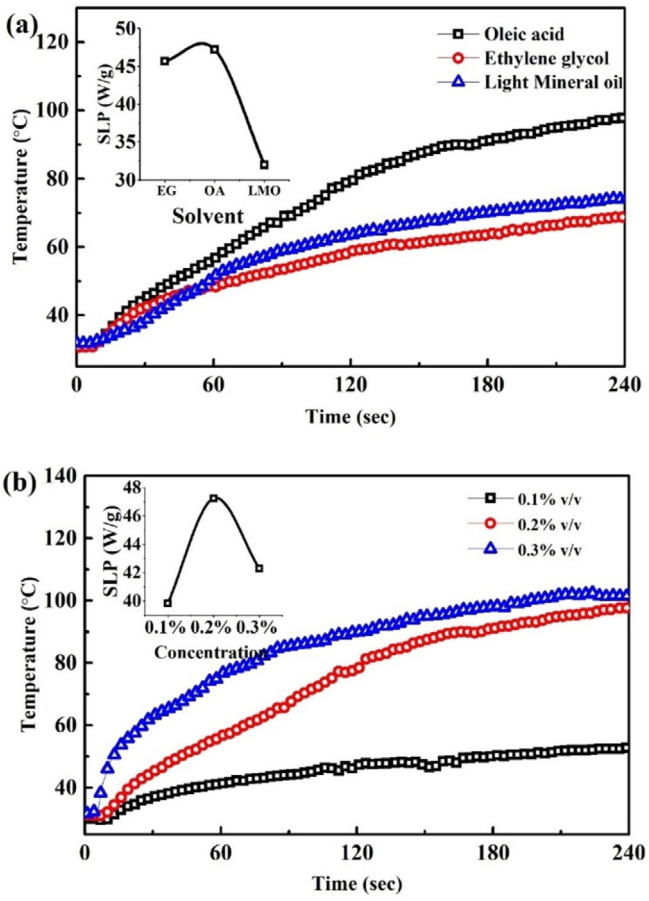

Figure 7. a) Temperature rise of iron nanoparticles dispersed in solvents of oleic acid, ethylene glycol, and mineral oil as a function of time under an AC magnetic field. The inset shows the change in SLP with type of solvent. b) Temperature rise of iron nanoparticles dispersed in oleic acid as a function of time under an AC magnetic field with concentrations of 0.1, 0.2, and 0.3% (*v*/*v*). The inset shows the change in SLP with nanoparticle concentration in oleic acid.

As the Fe nanoparticles in OA showed a maximum SLP, the effect of particle concentration on SLP was investigated by using OA as the solvent. Three concentrations were prepared, that is, 0.1, 0.2, and 0.3% (*v*/*v*). As expected, with an increase in the Fe nanoparticle concentration, the maximum temperature attained under the AMF also increased (Figure 7b). After 240 s, it was observed that the 0.2% (*v*/*v*) sample and the 0.3% (*v*/*v*) sample reached the same maximum temperature of about 98 °C. Interestingly, it was observed that the 0.2% (*v*/*v*) sample exhibited higher SLP than the 0.1 and 0.3% (*v*/*v*) samples (inset of Figure 7b). The initial slope was higher in the 0.3% (*v*/*v*) sample, but the mass of Fe nanoparticles was also higher in this sample; hence, the resultant SLP was less than that of the 0.2% (*v*/*v*) sample but higher than that of the 0.1% (*v*/*v*) sample. Particle concentration plays a crucial role in tailoring the heating efficiency. An increase in the concentration corresponds to a decrease in the mean interparticle separation and gives rise to a notable increase in the dipolar interparticle

interactions. The role that dipolar interactions might have in SLP is not completely understood at present,[70] but recent experimental studies suggest either an increase or decrease in SLP with interactions.[71] There are many factors that influence the heating ability of nanoparticles in suspensions, for example, specific heat of the solvent and particle dipole interactions.[72,73] The particle–particle separation can be affected by the strain induced on the nanoparticle surface due to the solvent.[74] The resultant SLP comes out to be a combination of all such factors.

The size of the magnetic nanoparticles and the viscosity of the medium fluid play important roles in heat generation. For small-sized nanoparticles, heat generation occurs through two main relaxation mechanisms:[75] 1) the Neel relaxation mechanism, which is due to a change in the magnetic moment of the nanoparticles with an external magnetic field in a finite time; 2) the Brownian relaxation mechanism, which occurs due to rotation of the entire particle in the magnetic field. Neel relaxation and Brownian relaxation dominate for small- and large-sized nanoparticles, respectively. The size distribution of our nanoparticles is broad, and therefore, heat generation may occur through either mechanism. The Brownian relaxation time is directly proportional to the viscosity of the fluid medium, as nanoparticles take a longer time to rotate physically in highly viscous fluids. The viscosity of the medium fluids is at a maximum in oleic acid (OA) and at a minimum in light mineral oil (LMO). Hence, the possibility that the Neel relaxation mechanism occurs may be higher in OA than in LMO or ethylene glycol (EG).

3. Conclusions

Iron and cobalt nanoparticles were synthesized by mechanochemical processing of a mixture of the corresponding oxides and Ca, followed by removal of the byproduct. The magnetic properties of these nanoparticles were measured with and without CaO. The Curie temperatures of the Fe and Co nanoparticles were found to be 923 and $\geq$1273 K, respectively. The mean blocking temperatures for the Fe and Co nanoparticles were found to be 29 and 163 K, respectively. The iron nanoparticles were fount to exhibit promising heating ability with a specific loss in power of 47 W g^{-1} at a low frequency and field strength. This mechanochemical method can be readily extended to the synthesis of other magnetic and nonmagnetic nanoparticles.

Experimental Section

Commercially available Fe_2O_3 (99.9%, Sigma Aldrich) and CoO (99.9%, Alfa Aesar) powders and Ca granules (99.9%, Sigma Aldrich) were used without further treatment. Prior to synthesis, CaO powder (99.9% Sigma Aldrich), which served as a dispersant, was heated at 1000 °C for 10 h to remove moisture.

For the iron samples, the quantity of precursors was determined by the following equation [Eq. (4)]:

$$Fe_2O_3 + 3\,Ca \rightarrow 2\,Fe + 3\,CaO \quad (4)$$

A 50 wt% excess amount of Ca granules above the stoichiometric amount was added to ensure full reduction. 40% CaO was added as a dispersant to reduce the reduction rate. In our recent study of NdFeCoB magnetic nanoparticles, we studied the effect of dispersant (CaO) ranging from 0 to 75% and the kinetics of mechanochemical synthesis.[21,37] We observed that adding CaO was helpful to control the reaction and resulted in better magnetic properties than samples without CaO. Most of the previous studies also included the corresponding dispersing agent to control the self-sustaining reaction. Adding CaO was helpful to control the self-sustaining reaction and also to make it easy to remove the powder from the walls of the milling bowls. Another reason to add CaO was to prepare an appropriate mass fraction of metal to CaO (Fe/Cao and Co/CaO) for catalyst applications.[76] Fe_2O_3 and CaO powders were mixed in a mortar by hand grinding before loading into a milling vial. The powder of mixed Fe_2O_3 and CaO along with Ca granules were sealed in a tungsten carbide milling vial in a glovebox filled with Ar gas (H_2O and O_2 levels less than 10 ppm).

For the cobalt samples, the quantity of precursors was determined by the following equation [Eq. (5)]:

$$CoO + Ca \rightarrow Co + CaO \quad (5)$$

Again, a 50 wt% excess amount of Ca granules was added. The mixed powder of CoO and CaO and Ca granules were sealed in a tungsten carbide milling vial in an argon glovebox. The reaction $Fe_2O_3 + 3\,Ca \rightarrow 2\,Fe + 3\,CaO$ has an enthalpy of reaction (ΔH) value of -1081 kJ. The reaction $CoO + Ca \rightarrow Co + CaO$ has a ΔH value of -342 kJ. Such large values for enthalpy change can significantly increase the local temperature.[26]

The experimental parameters for mechanochemical synthesis of iron and cobalt nanoparticles were identical. Ball-to-powder ratio, milling speed, milling time, milling atmosphere, and heat treatment conditions were the same for both cases. The milling process was conducted in a Fritch Pulverisette-7 planetary ball mill at a milling speed of 500 rpm for 6 h, with a ball-to-powder ratio of 14:1. After milling, the black powder was collected in an argon glovebox and pressed into a pellet by using a hydraulic press to minimize exposure of the powder to air. This pellet was heat treated in a tube furnace at 850 °C for 90 min under high vacuum ($\approx 10^{-5}$ Torr). The heat-treated sample could then be handled in air. The sample was subsequently washed with NH_4Cl dissolved in methanol for 30 min to remove CaO, which was followed by vacuum drying. The reaction for removal of Cao from the Fe/CaO nanocomposite may be [Eq. (6)]:

$$2\,NH_4Cl + Fe + CaO + CH_3OH \rightarrow Fe + CaCl_2 + 2\,NH_3 + CH_3OH + H_2O \quad (6)$$

A schematic of the process, from precursors to product, is shown in Figure 8.

X-ray diffraction data for all samples were collected by using a Bruker D8 X-ray diffractometer (CuKα radiation; wavelength = 0.154 nm) and were analyzed by using Rietveld refinement via the Topas 4.1 program. Rietveld refinement was performed by assuming that the samples did not contain an amorphous phase. To determine the particle size and morphology, transmission electron microscopy (TEM) was performed with a JEOL 2010 TEM with an operating voltage of 200 kV. Samples were prepared by ultrasonically dispersing a small quantity of powder in ethanol, followed by

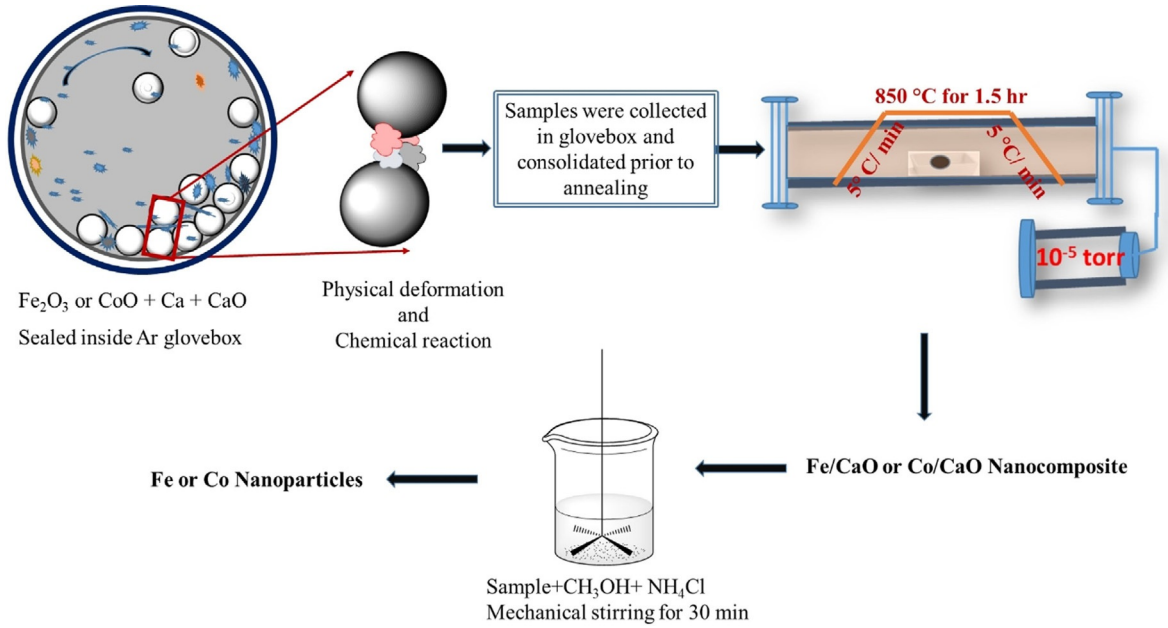

Figure 8. Schematic of the mechanochemical process for the synthesis of Fe and Co nanoparticles and the Fe/CaO and Co/CaO nanocomposites.

placing a drop of the suspension on a holey carbon-coated copper grid. The sample was then dried overnight in air. Elemental mapping analysis was performed by scanning electron microscopy (SEM, JEOL 6360) with an energy-dispersive X-ray spectrometer (EDX) operating at 15 kV. The magnetic properties were measured by a Lakeshore 7407 vibrating sample magnetometer (VSM) for magnetic fields up to 15 kOe. The zero-field-cooled (ZFC) and field-cooled (FC) magnetization curves were measured in the temperature range of 10 to 400 K at an applied magnetic field of 100 Oe by using a physical properties measurement system (EverCool-II, Quantum Design, USA) equipped with a vibrating sample magnetometer attachment. The ZFC measurements were performed by applying a magnetic field of 100 Oe after the sample was cooled in zero field. FC curves were obtained after cooling the sample in an applied field of 100 Oe. To determining the efficiency of heating these nanoparticles, an alternating magnetic field of strength 4 kA m^{-1} and frequency of 375 kHz was employed.

Magnetic nanoparticles suspended in solvent contained in a glass bottle were placed inside a water-cooled five-loop copper induction coil energized by an AC generator (Inductelec, UK) with an operating frequency of 375 kHz and a field strength of 4 kA m^{-1}. The frequency could not be changed in our system. Moreover, for hyperthermia applications, good heating efficiency at low frequency is advisable.[77] Usually, with increasing frequency, the specific loss in power (SLP) increases in a linear manner if the applied field constant is kept constant.

Acknowledgements

This research was supported by grants from the National Research Foundation, Prime Minister's Office, Singapore, under its Campus of Research Excellence and Technological Enterprise (CREATE) program.

Conflict of Interest

The authors declare no conflict of interest.

Keywords: cobalt · iron · nanoparticles · magnetization · mechanochemistry

[1] A. H. Lu, E. L. Salabas, F. Schüth, *Angew. Chem. Int. Ed.* **2007**, *46*, 1222 – 1244; *Angew. Chem.* **2007**, *119*, 1242 – 1266.
[2] N. A. Frey, S. Peng, K. Cheng, S. Sun, *Chem. Soc. Rev.* **2009**, *38*, 2532 – 2542.
[3] S. Singamaneni, V. N. Bliznyuk, C. Binek, E. Y. Tsymbal, *J. Mater. Chem.* **2011**, *21*, 16819 – 16845.
[4] R. Hudson, Y. Feng, R. S. Varma, A. Moores, *Green Chem.* **2014**, *16*, 4493 – 4505.
[5] V. Chaudhary, R. V. Ramanujan, *MRS Online Proc. Libr.* **2014**, *1708*, vv10-08.
[6] A. Ray, V. Chaudhary, Z. Wang, R. Ramanujan, *J. Nanofluids* **2016**, *5*, 783 – 789.
[7] D. L. Huber, *Small* **2005**, *1*, 482 – 501.
[8] M. M. Yallapu, S. F. Othman, E. T. Curtis, B. K. Gupta, M. Jaggi, S. C. Chauhan, *Biomaterials* **2011**, *32*, 1890 – 1905.
[9] W. Wu, Z. Wu, T. Yu, C. Jiang, W.-S. Kim, *Sci. Technol. Adv. Mater.* **2015**, *16*, 023501.
[10] V. Chaudhary, Z. Wang, A. Ray, I. Sridhar, R. V. Ramanujan, *J. Phys. D* **2017**, *50*, 03LT03.
[11] V. Chaudhary, R. V. Ramanujan, *Sci. Rep.* **2016**, *6*, 35156.
[12] V. F. Puntes, K. M. Krishnan, A. P. Alivisatos, *Science* **2001**, *291*, 2115 – 2117.
[13] S. A. Salman, T. Usami, K. Kuroda, M. Okido, *J. Nanotechnol.* **2014**, *2014*, 525193.
[14] S. R. Mallampati, Y. Mitoma, T. Okuda, C. Simion, B. K. Lee, *J. Hazard. Mater.* **2015**, *297*, 74 – 82.
[15] C. B. Rong, D. Wang, V. Van Nguyen, M. Daniil, M. A. Willard, Y. Zhang, M. J. Kramer, J. P. Liu, *J. Phys. D* **2013**, *46*, 045001.
[16] S. Tong, C. A. Quinto, L. Zhang, P. Mohindra, G. Bao, *ACS Nano* **2017**, *11*, 6808 – 6816.

[17] V. Patsula, M. Moskvin, S. Dutz, D. Horák, *J. Phys. Chem. Solids* **2016**, *88*, 24 – 30.
[18] P. S. Owuor, V. Chaudhary, C. F. Woellner, V. Sharma, R. V. Ramanujan, A. S. Stender, M. Soto, S. Ozden, E. V. Barrera, R. Vajtai, D. S. Galvão, J. Lou, C. S. Tiwary, P. M. Ajayan, *Mater. Today.* **2018**, *21*, 475 – 482.
[19] J. R. Thomas, *J. Appl. Phys.* **1966**, *37*, 2914 – 2915.
[20] S.-J. Park, S. Kim, S. Lee, Z. G. Khim, K. Char, T. Hyeon, *J. Am. Chem. Soc.* **2000**, *122*, 8581 – 8582.
[21] Y. Zhong, V. Chaudhary, X. Tan, H. Parmar, R. V. Ramanujan, *Nanoscale* **2017**, *9*, 18651 – 18660.
[22] L. Takacs, *Chem. Soc. Rev.* **2013**, *42*, 7649 – 7659.
[23] Q. Zhang, F. Saito, *Adv. Powder Technol.* **2012**, *23*, 523 – 531.
[24] J.-K. Noh, S. Kim, H. Kim, W. Choi, W. Chang, D. Byun, B.-W. Cho, K. Y. Chung, *Sci. Rep.* **2014**, *4*, 4847.
[25] T. Tsuzuki, P. G. McCormick, *J. Mater. Sci.* **2004**, *39*, 5143 – 5146.
[26] J. Ding, T. Tsuzuki, P. G. McCormick, R. Street, *J. Alloys Compd.* **1996**, *234*, L1 – L3.
[27] J. Ding, T. Tsuzuki, P. G. McCormick, *J. Am. Ceram. Soc.* **1996**, *79*, 2956 – 2958.
[28] J. Ding, T. Tsuzuki, P. G. McCormick, *Nanostruct. Mater.* **1997**, *8*, 75 – 81.
[29] H. M. Yang, X. C. Zhang, A. D. Tang, W. Q. Ao, *Mater. Sci. Technol.* **2004**, *20*, 1493 – 1495.
[30] M. Seyedi, S. Haratian, J. V. Khaki, *Procedia Mater. Sci.* **2015**, *11*, 309 – 313.
[31] M. Pardavi-Horvath, L. Takacs, *J. Appl. Phys.* **1993**, *73*, 6958 – 6960.
[32] M. Pardavi-Horvath, L. Takacs, *Scr. Metall. Mater.* **1995**, *33*, 1731 – 1740.
[33] M. Pardavi-Horvath, L. Takacs, *IEEE Trans. Magn.* **1992**, *28*, 3186 – 3188.
[34] L. Takacs, M. Pardavi-Horvath, *J. Appl. Phys.* **1994**, *75*, 5864 – 5866.
[35] R. Sibul, E. Kibena-Põldsepp, S. Ratso, M. Kook, M. Käärik, M. Merisalu, P. Paiste, J. Leis, V. Sammelselg, K. Tammeveski, *Electrochem. Commun.* **2018**, *93*, 39 – 43.
[36] S. Ostovar, A. Franco, A. R. Puente-Santiago, M. Pinilla-de Dios, D. Rodríguez-Padrón, H. R. Shaterian, R. Luque, *Front. Chem.* **2018**, *6*, 77; https://doi.org/10.3389/fchem.2018.00077.
[37] Y. Zhong, V. Chaudhary, X. Tan, H. Parmar, R. V. Ramanujan, *J. Alloys Compd.* **2018**, *747*, 755 – 763.
[38] V. Chaudhary, Y. Zhong, H. Parmar, X. Tan, R. Ramanujan, *ChemPhysChem* **2018**, https://doi.org/10.1002/cphc.201800318.
[39] Q. Li, Y. Li, Y. Chen, L. Wu, C. Yang, X. Cui, *Carbon* **2018**, *136*, 248 – 254.
[40] H. Wang, J. B. DeLisio, T. Wu, X. Wang, M. R. Zachariah, *Powder Technol.* **2018**, *324*, 62 – 68.
[41] E. Dutková, Z. Bujňáková, J. Kováča, I. Škorvánek, M. J. Sayagués, A. Zorkovská, J. Kováč, P. Baláž, *Adv. Powder Technol.* **2018**, *29*, 1820 – 1826.
[42] D. Davoodi, A. H. Emami, M. Tayebi, S. K. Hosseini, *Ceram. Int.* **2018**, *44*, 5411 – 5419.
[43] M. H. Baradaran-Ghandi, S. A. Hassanzadeh-Tabrizi, *Ceram. Int.* **2018**, *44*, 5447 – 5452.
[44] I. Y. Ta, C. Su-Hua, *Nanotechnology* **2017**, *28*, 055601.
[45] J. Ding, T. Tsuzuki, P. G. McCormick, R. Street, *J. Phys. D* **1996**, *29*, 2365.
[46] J. Ding, W. F. Miao, P. G. McCormick, R. Street, *Appl. Phys. Lett.* **1995**, *67*, 3804 – 3806.
[47] I. Zamboni, C. Courson, A. Kiennemann, *Catal. Today* **2011**, *176*, 197 – 201.
[48] A. M. Stoneham, *J. Phys. C* **1977**, *10*, 1175.
[49] B. D. Cullity, *Elements of X-ray Diffraction*, Addison-Wesley, Massachusetts, **1956**.
[50] V. Chaudhary, A. K. Srivastava, J. Kumar, *MRS Online Proc. Libr.* **2011**, 1352.
[51] C. C. Koch, *Nanostruct. Mater.* **1993**, *2*, 109 – 129.
[52] P. G. McCormick, T. Tsuzuki, J. S. Robinson, J. Ding, *Adv. Mater.* **2001**, *13*, 1008 – 1010.
[53] H. Yang, Y. Hu, A. Tang, S. Jin, G. Qiu, *J. Alloys Compd.* **2004**, *363*, 276 – 279.
[54] T. Tsuzuki, E. Pirault, P. G. McCormick, *Nanostruct. Mater.* **1999**, *11*, 125 – 131.
[55] D. A. Garanin, H. Kachkachi, *Phys. Rev. Lett.* **2003**, *90*, 065504.
[56] V. Chaudhary, D. V. Maheswar Repaka, A. Chaturvedi, I. Sridhar, R. V. Ramanujan, *J. Appl. Phys.* **2014**, *116*, 163918 – 163926.
[57] S. A. Kahani, M. Khedmati, *J. Nanomater.* **2015**, 246254.
[58] W. H. Zhong, Q. S. Chang, B. K. Tay, S. Li, H. L. Bai, E. Y. Jiang, *J. Phys. Condens. Matter* **2002**, *14*, L399.
[59] X. He, W. Zhong, C.-T. Au, Y. Du, *Nanoscale Res. Lett.* **2013**, *8*, 446.
[60] R. Evans, U. Nowak, F. Dorfbauer, T. Shrefl, O. Mryasov, R. W. Chantrell, G. Grochola, *J. Appl. Phys.* **2006**, *99*, 08G703.
[61] W. Wu, X. Xiao, S. Zhang, T. Peng, J. Zhou, F. Ren, C. Jiang, *Nanoscale Res. Lett.* **2010**, *5*, 1474.
[62] S. Dey, R. Mondal, S. K. Dey, S. Majumder, P. Dasgupta, A. Poddar, V. R. Reddy, S. Kumar, *J. Appl. Phys.* **2015**, *118*, 103905.
[63] H. Parmar, P. Acharya, R. V. Upadhyay, V. Siruguri, S. Rayaprol, *Solid State Commun.* **2013**, *153*, 60 – 65.
[64] C. de Julián Fernández, *Phys. Rev. B.* **2005**, *72*, 054438.
[65] H. T. Yang, C. M. Shen, Y. K. Su, T. Z. Yang, H. J. Gao, Y. G. Wang, *Appl. Phys. Lett.* **2003**, *82*, 4729 – 4731.
[66] M. Bekovic, A. Hamler, *IEEE Trans. Magn.* **2010**, *46*, 552 – 555.
[67] M. Gonzales-Weimuller, M. Zeisberger, K. M. Krishnan, *J. Magn. Magn. Mater.* **2009**, *321*, 1947 – 1950.
[68] A. Skumiel, *J. Magn. Magn. Mater.* **2006**, *307*, 85 – 90.
[69] M. Zeisberger, S. Dutz, R. Müller, R. Hergt, N. Matoussevitch, H. Bönnemann, *J. Magn. Magn. Mater.* **2007**, *311*, 224 – 227.
[70] F. Burrows, C. Parker, R. F. L. Evans, Y. Hancock, O. Hovorka, R. W. Chantrell, *J. Phys. D* **2010**, *43*, 474010.
[71] C. L. Dennis, A. J. Jackson, J. A. Borchers, P. J. Hoopes, R. Strawbridge, A. R. Foreman, J. van Lierop, C. Grüttner, R. Ivkov, *Nanotechnology* **2009**, *20*, 395103.
[72] M. Jeun, S. Bae, A. Tomitaka, Y. Takemura, K. H. Park, S. H. Paek, K.-W. Chung, *Appl. Phys. Lett.* **2009**, *95*, 082501.
[73] C. Haase, U. Nowak, *Phys. Rev. B* **2012**, *85*, 045435.
[74] R. Ghosh, L. Pradhan, Y. P. Devi, S. S. Meena, R. Tewari, A. Kumar, S. Sharma, N. S. Gajbhiye, R. K. Vatsa, B. N. Pandey, R. S. Ningthoujam, *J. Mater. Chem.* **2011**, *21*, 13388 – 13398.
[75] G. Seshadri, R. Thaokar, A. Mehra, *J. Magn. Magn. Mater.* **2014**, *362*, 165 – 171.
[76] L. Sun, X. Zhang, L. Chen, B. Zhao, S. Yang, X. Xie, *J. Anal. Appl. Pyrolysis* **2016**, *119*, 133 – 138.
[77] S. Purushotham, R. V. Ramanujan, *Acta Biomater.* **2010**, *6*, 502 – 510.

Received: May 20, 2018
Revised manuscript received: June 16, 2018

